Nanoscale

Accepted Manuscript

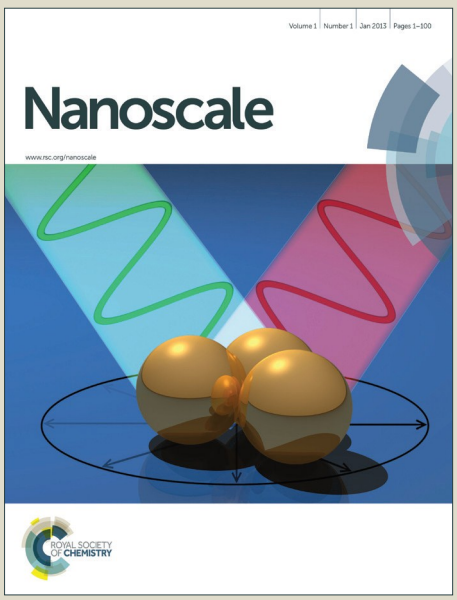

ROYAL SOCIETY OF CHEMISTRY

www.rsc.org/nanoscale

Nanoscale

Paper

Rational Assembly of Biointerfaced Core@Shell Nanocomplex towards Selective and Highly Efficient Synergistic Photothermal/Photodynamic Therapy

Received 00th January 20xx,
Accepted 00th January 20xx

DOI: 10.1039/x0xx00000x

www.rsc.org/

Chenchen Qin,[a] Jinbo Fei,[a] Anhe Wang,[b] Yang Yang,[b] and Junbai Li [a,b]*

Abstract: To optimize synergistic cancer therapy, we rationally assemble an inorganic-organic nanocomplex using folate-modified lipid bilayer spread on photosensitizer-entrapped mesoporous silica nanoparticle (MSN) coated gold nanorod (AuNR). In this hybrid bioconjugate, the large specific surface area and pore size of AuNR@MSN guarantees a high loading capacity of small photosensitive molecules. The modification with selective mixed liposomes on the surface of AuNR@MSN enables faster cellular internalization and enhancement of endocytosis. Under one-time NIR two-photon illumination, AuNR-mediated hyperthermia can kill cancer cells directly. Meanwhile, the loaded photosensitizer, hypocrellin B, generates two kinds of reactive oxygen species (ROS) to induce cell apoptosis. Remarkably, hyperthermia can improve the yield of ROS. After intravenous injection of this bioconjugate to female BALB/c nude mice followed by laser irradiation (808 nm, 1.3 W/cm^2, 6 min), the tumor growth is suppressed completely. The tumors are not recurrent within the observation time (19 days), and the normal or main organs are not obviously pathological. Thus, such a simplified and selective cancer treatment, combining photothermal and photodynamic therapy in a synergistic manner, provides outstanding efficiency *in vivo*. The nanocomplex with well-defined core@shell nanostructure connected with a two-photon technique holds a great promise to improve cancer phototherapy with high efficiency in the clinic.

Introduction

Systematic combination of different anticancer treatments such as radiotherapy, chemotherapy and phototherapy can diminish drawbacks of individual methods and optimize efficiency.[1-5] Recently, novel nanocomplexes have attracted increasing attention because of their advanced physical, chemical and biological properties, compared to traditional medicine.[6-12] However, it is still a great challenge to design and construct well-defined nanostructures to assemble multicomponent systems in order to achieve the most intelligent combination for selective and synergistic cancer therapy.

Among present anticancer treatments, phototherapy including photothermal therapy (PTT) and photodynamic therapy (PDT) possesses obviously outstanding advantages, such as few side effects, low toxicity and remote controllability, especially avoiding chemo-resistance. The development of PTT and PDT heavily depends on photothermal and photosensitive agents. Near-infrared (NIR) illumination phototherapy is ideal for real applications because of the large penetration depth.[13, 14] Up to now, many kinds of photothermal sensitizers with high-absorption cross section for conversion of NIR light into heat have been fabricated, such as gold nanostructures,[15-21] carbon nanotubes,[22-24] and graphene oxide.[25-27] Among them, gold nanostructures, as optimum photothermal agents with a tuneable localized surface plasmon resonance (LSPR) between 750 and 950 nm, are considered to have great potential for combined PTT and PDT.[29-36] For instance, Lin and co-workers described a vesicle containing aggregated gold nanoparticles and photosensitizer Chlorin e6 (Ce6) for PTT and PDT using two continuous lasers.[29] Also, Hwang and colleagues reported the combined PTT and PDT for enhanced cancer treatment using gold nanoshells alone as both photothermal agent and photosentisizer.[30] Unfortunately, on one hand, the LSPR peak of gold nanostructures could be shifted to the visible spectral region because of their easy clustering and aggregation upon NIR laser illumination,[37-39] resulting in low efficiency of phototherapy in the NIR window. In order to overcome this weakness, some hard substances like mesoporous silica nanoparticles (MSN) were deposited on gold nanostructures.[1, 6] On the other hand, although there have been excellent photosensitizers such as porphyrins and phthalocyanines (Ce6, $AlPcS_4$ and $ZnPcS_2P_2$) widely used for PDT,[29-36] only few photosensitizers can be excited to generate reactive oxygen species (ROS) using continuous wave NIR laser.[40] Considering the mismatch of excited wavelength between gold nanostructures and photosensitizer, it would be very difficult

[a] Beijing National Laboratory for Molecular Sciences, CAS Key Lab of Colloid, Interface and Chemical Thermodynamics, Institute of Chemistry, Chinese Academy of Sciences, Beijing, 100190, China, E-mail: jbli@iccas.ac.cn.
[b] National Center for Nanoscience and Technology, Beijing, 100190, China.
†Electronic Supplementary Information (ESI) available: The relevant TEM, DLS, UV, photograph and chemical structures. See DOI: 10.1039/x0xx00000x

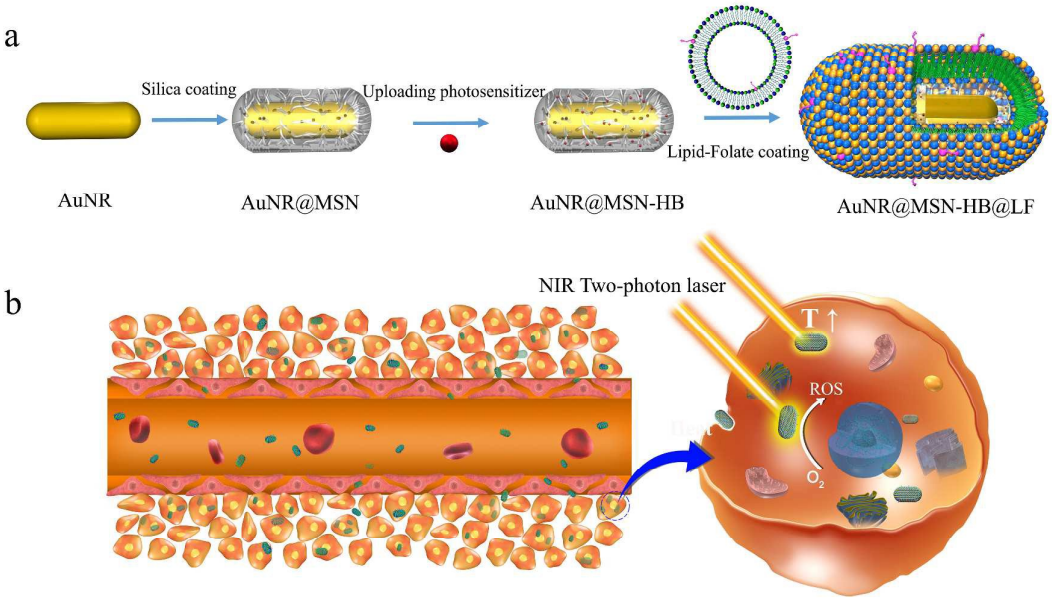

Scheme 1 (a) The formulation process of the biointerfaced nanocomplex. AuNR was coated by a mesoporous silica film incorporating photosensitizer and a folate-modified lipid bilayer to form the bioconjugate with well-defined nanostructure (AuNR@MSN-HB@LF). (b) Combined treatment of two-photon photothermal/photodynamic therapy for inhibiting tumor cell growth. After preferably internalized by tumor cells, under one-time irradiation with a two-photon NIR laser, hyperthermia and ROS induced by the bioconjugate generate in a synergistic manner to kill tumor cells with high efficiency.

to achieve a highly efficient combination of PTT and PDT under a single traditional NIR laser illumination.

In the present work, under the assistance of two-photon technique, we construct a biointerfaced nanocomplex with selective recognition that couples PTT and PDT in a one-time synergistic manner, as illustrated in Scheme 1a. Firstly, AuNRs were prepared by a seed-induced-growth method.[41, 42] Then, MSN with high specific surface area were deposited on the surface of gold nanorod (AuNR) to form core-shell AuNR@MSN.[43-45] Subsequently, hypocrellin B (HB, Fig. S1†), as a typical photodynamic therapeutic agent in the visible region, was incorporated into the MSN shell. Finally, folate-modified lipid (LF) vesicles were allowed to spread on the outside of AuNR@MSN-HB to assemble the bioconjugate AuNR@MSN-HB@LF. The LF on the surface can guide the nanocomplex into cells and remarkably increase the effective accumulation in tumor region, which will be shown to enhance cancer treatment. As presented in Scheme 1b, under one-time illumination by a single femtosecond laser (808 nm), AuNR eventually induce a temperature rise and HB as photosensitizer is initiated to generate ROS. Significantly, the yield of ROS can be improved by hyperthermia. After intravenous injection and following phototherapy (PTT and PDT) *in vivo*, the tumor is considerably inhibited. The simplified operation can be manipulated precisely and readily. Thus, by integrating the two-photon technique, such a "soft-hard" hybrid nanocomplex with selective recognition provides an excellent approach to realize highly efficient cancer phototherapy *in vitro* and *in vivo*.

Results and Discussion

Preparation and Characterization of the Biointerfaced Nanocomplex

AuNRs were synthesized according to a reported protocol with minor modification.[41, 42] Transmission electron microscopy (TEM) image in Fig. 1a reveals that AuNRs are about 60 nm in length and 15 nm in width, respectively. It can be supported by the relevant statistical results (Fig. S2†). A mesoporous silica layer was introduced by the Stöber method to form core-shell AuNR@MSN in order to incorporate photosensitizer molecules. As revealed in Fig. 1b, the coated mesoporous silica shell possesses a homogeneous thickness of about 30 nm and disordered pores with the mean diameter around 3 nm (Fig. S3a, b†), offering a chance for AuNR@MSN serving as a drug carrier. Moreover, Brunauer-Emmett-Teller (BET) analysis yields an average pore width of about 28 Å (shown in Fig. 1c) which is large enough to adsorb the small photosensitizer HB (~1 nm). In addition, the inset in Fig. 1c displays a high specific surface area of 231.4 m^2/g. It implies AuNR@MSN has a potential high adsorption capacity for HB. As a result, loading efficiency amounts to 44% by comparing absorbance in HB solution before and after adsorption (Fig. 1d). Based on further analysis of Au content by inductively coupled plasma mass

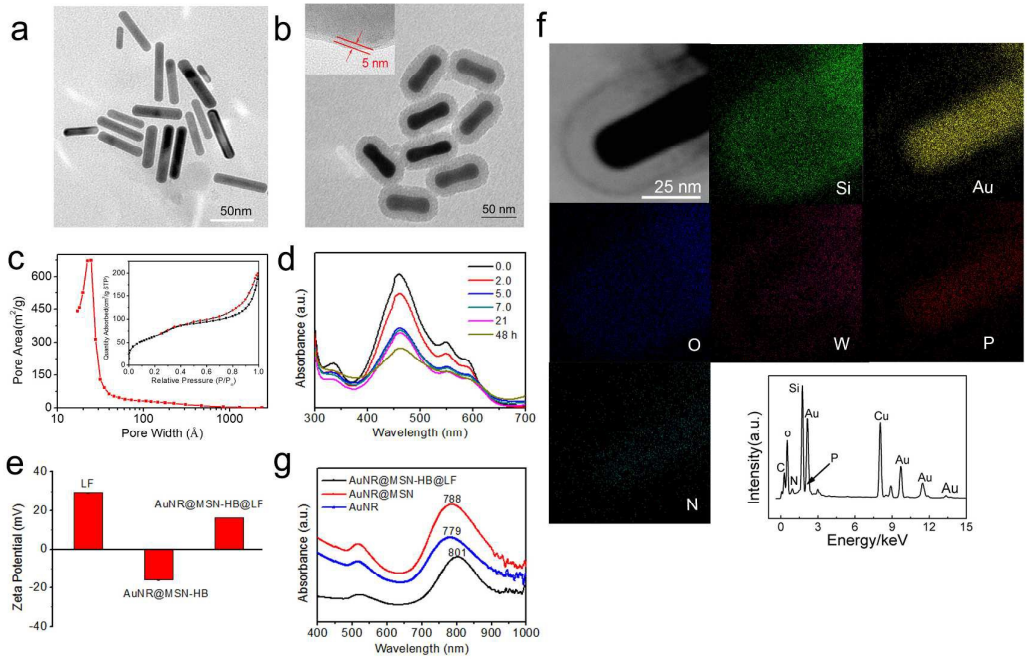

Fig. 1 TEM images of (a) AuNR and (b) AuNR@MSN. The inset is the edge of the bioconjugate AuNR@MSN-HB@LF stained with 1% phosphotungstic acid. (c) The pore distribution of AuNR@MSN. The inset is relevant N_2 adsorption-desorption isotherms. (d) UV-vis spectra of HB after adsorption by AuNR@MSN as a function of time. (e) Zeta potentials of LF, AuNR@MSN-HB, and AuNR@MSN-HB@LF. (f) EDX mapping and pattern of the bioconjugate. (g) UV-vis spectra of AuNR, AuNR@MSN and AuNR@MSN-HB@LF.

spectrometry (ICP-MS), 1 mg AuNR@MSN-HB contains 420 μg Au and 22.5 μg HB.

In order to enhance the effective accumulation of the bioconjugate in the tumour region, a lipid bilayer with selective recognition was deposited on the surface of AuNR@MSN-HB to form the final bioconjugate AuNR@MSN-HB@LF. The lipid bilayer is composed of 1, 2-dioleoyl-sn-glycero-3-phosphoethanolamine (DOPE), 1, 2-dioleoyl-3-trimethylammonium-propane (DOTAP), 1, 2-distearoyl-sn-glycero-3-phosphoethanolamine-N-[folate (polyethylene glycol)-2000] (DSPE-PEG(2000)-Folate) and cholesterol. Their chemical structures are shown in Fig. S4†. The diameter of the mixed liposomes is about 165 nm (Fig. S5a, b†). From Fig. S3c† and the inset in Fig. 1b, we deduce that in the assembled nanocomplex, AuNR@MSN-HB is surrounded by a continuous soft layer with a lower electron density, most probably the lipid bilayer. From TEM image with higher magnification (Fig. S3d†), the thickness of the soft layer can be estimated to about 5 nm, which is consistent with that of a lipid bilayer.[43, 44] Furthermore, zeta potentials of AuNR@MSN-HB and LF were -16.1 and 29.4 mV, respectively (Fig. 1e). It indicates that negatively-charged AuNR@MSN-HB could be readily coated with positively-charged liposomes by electrostatic interaction.[43-45] Consequently, the zeta potential of AuNR@MSN-HB@LF was 16.2 mV. As shown in Fig. 1f, energy dispersive X-ray (EDX) pattern yields the elemental components in the bioconjugate, Au, Si, O, C, N, P, W and Cu. Moreover, the mapping analysis of a single nanoparticle with 1% phosphotungstic acid staining exhibits well-defined core@shell nanostructures, confirming the lipid bilayer coating to AuNR@MSN-HB is successful.

Fig. 1g reveals the SPR characteristics of AuNR, AuNR@MSN and AuNR@MSN-HB@LF, respectively. The as-prepared AuNR has a typical longitudinal SPR peak at 779 nm. Red shifts appear after coating, which is due to the change in the local refractive index.[46] AuNR@MSN-HB@LF has a longitudinal SPR peak at 801 nm, which promises further PTT under NIR illumination. Without a silica shell, AuNR alone can aggregate easily, leading to a considerable blue shift of the LSPR adsorption peak (Fig. S6†). As a comparison, the stability of the bioconjugate in buffer solution and serum containing medium are much better (shown in Fig. S7†). This confirms that it is very important and necessary to coat AuNR.

Photothermal and Photodynamic Effects

In order to optimize the conditions for cancer treatment *in vitro* and *in vivo*, two main factors (concentration of the bioconjugate and irradiation power density) influencing on the photothermal effect were investigated. AuNR@MSN-HB@LF with different concentrations (0, 12.5, 25, 50, 75 and 100 μg/mL) was irradiated by the 808 nm fs laser (1.5 W/cm^2). The results quantify that in all cases, temperature increases along with irradiation time, as shown in Fig. 2a. In particular, for 12.5 μg/mL AuNR@MSN-HB@LF after irradiation for 5 min, the temperature increased by about 15 ^{o}C, which is sufficient to

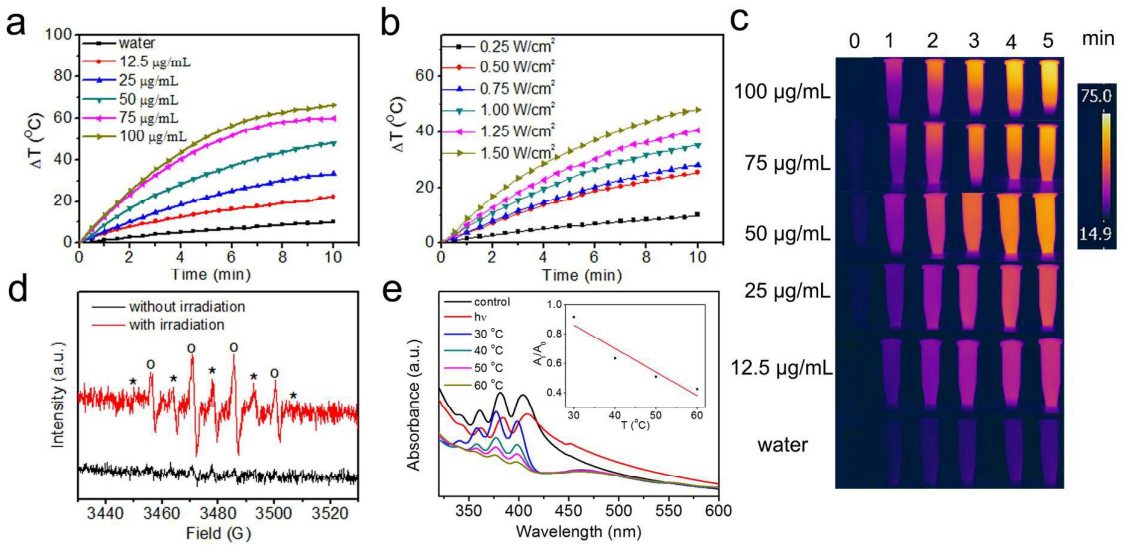

Fig. 2 (a) Time-dependent temperature change of AuNR@MSN-HB@LF dispersion with different concentrations. The samples were irradiated with a NIR laser (808 nm) at the power density of 1.5 W/cm^2. The water was used as the control group. (b) Time-dependent temperature change at the different laser power density. The samples (15 μg/mL) were irradiated by the same laser above. (c) Temperature images of AuNR@MSN-HB@LF solution with different concentrations under a NIR laser (808 nm, 1.5 W/cm^2) irradiation recorded by infrared thermal camera. (d) ESR spectra of the radical spin adduct in AuNR@MSN-HB@LF aqueous solution with/without irradiation. (e) UV-vis spectra of DPA in H_2O-DMSO under darkness (black curve); upon irradiation at 475 nm for 5 min (red curve); together with LF-HB under the same irradiation condition above at 30 °C (blue curve), 40 °C (green curve), 50 °C (pink curve), and 60 °C (yellow curve), respectively. The final concentration of HB in the formulation is 45 μg/mL. A_t/A_0 represents the ratio of remnant DPA after irradiation at the designated temperature.

damage the tumor cell irreversibly.[4, 47] Likewise, the relevant results shown in Fig. 2b yield that the temperature rising rate and the final temperature are proportional to the laser power density. Furthermore, similar conclusions can also be drawn by analysing corresponding infrared thermal photographs (Fig. 2c). In addition, accompanying the increasing temperature, HB was released from the assembled nanocomplex (Fig. S8†). In contrast, without irradiation, in PBS (pH 7.2) or cell culture medium, there is no obvious leakage of HB from the nanocomposite before and after lipid coating (Fig. S9†).

Electron spin resonance (ESR) measurement was employed to detect ROS when AuNR@MSN-HB@LF was exposed to light illumination. As shown in Fig. 2d, signals marked with "o" are mainly ascribed to the reaction of 5, 5-dimethyl-1-pyrroline-N-oxide (DMPO) with ROS generated by HB. This produces the stable DMPO-hydroxyl radical spin adduct DMPO-OH, which yields a typical •OH signal.[49] Note that highly active radical •OH can attack adjacent carbon-centered organic compounds. As a result, carbon-centered radicals marked with "*" could be subsequently spin trapped by DMPO (Fig. 2d).[49-52] The two kinds of signals confirm the production of ROS. Generated ROS can cause irreversible damage to tumor cells in further PDT. Moreover, to preliminarily investigate the synergistic effect of hyperthermia on the yield of ROS, temperature-dependent absorbance decrease of 9,10-diphenylanthracene (DPA) resulted from the oxidation of by ROS was monitored.[50] As shown in Fig. 2e, the generated ROS was increased along with the increasing temperature.

Cellular Internalization

Confocal scanning microscopy (CLSM) was explored to define the endocytosis and the intracellular distribution of the nanocomplex. Michigan Cancer Foundation-7 (MCF-7) cells (a breast cancer cell line) with overexpressed folate receptors were incubated with the nanocomplex. Dark pots in Fig. 3aA (bright field) reveal the bioconjugate internalized. The red one-photon fluorescence and green two-photon luminescence in Fig. 3aB, C present the distribution of LysoTracker Red and AuNR in the cells, respectively. From the overlap image (Fig. 3aD), we deduce that a large number of nanocomplexes are localized in the lysosomal acidic compartment. The *in vitro* process could be proposed that after lipid fusion with cell membrane, LF departs from AuNR@MSN-HB@LF and remaining AuNR@MSN-HB enters into the lysosome.[53]

Effective accumulation of nanocomplexes in tumor cells is crucial for improving cancer therapy.[54] To demonstrate that LF is helpful for the nanocomplexes to be internalized by the tumor cells, the time-dependent Au contents in cells were measured by ICP-MS. In detail, AuNR@MSN-HB@LF and AuNR@MSN-HB with the same Au content were co-incubated with MCF-7 cells for 0.5, 1, 3, 6, and 9 h. As shown in Fig. 3b, the internalized Au content increases along with the

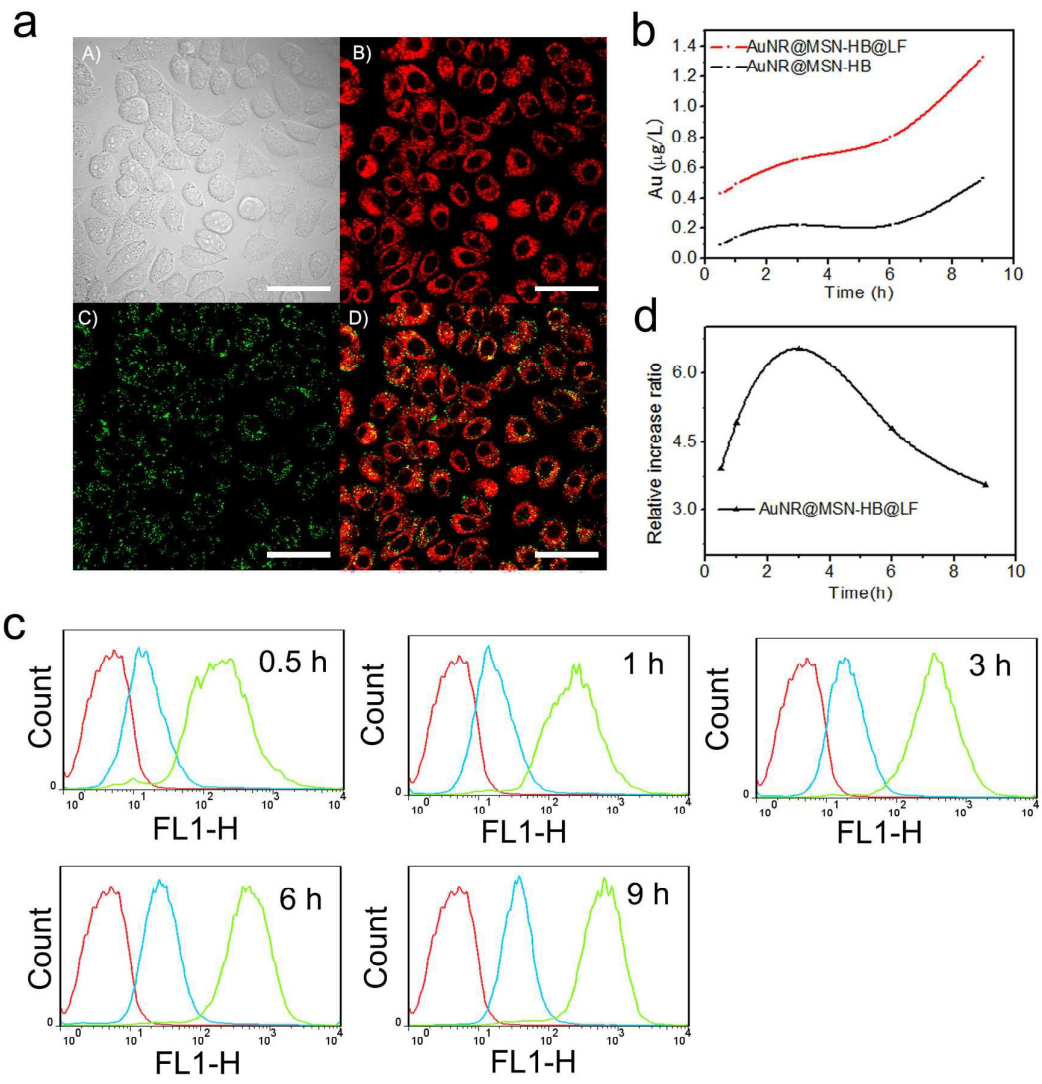

Fig. 3 (a) CLSM images of MCF-7 cells co-cultured with AuNR@MSN-HB@LF for 6 h. (A) bright field; (B) one-photon fluorescence from LysoTracker Red excited at 559 nm; (C) two-photon luminescence from AuNR excited by an 808 nm two-photon laser; (D) the relevant merge image. The scale bars are 50 μm. (b) The intercellular time-dependent content of Au after co-cultured with AuNR@MSN-HB@LF and AuNR@MSN-HB. (c) Corresponding flow cytometric analysis at different times (0.5, 1, 3, 6, 9 h). The control group without any nanoparticles (red); AuNR@MSN-HB (blue); AuNR@MSN-HB@LF (green). (d) The relative increase ratio of endocytosis amount of AuNR@MSN-HB@LF, compared to that of AuNR@MSN-HB.

incubation time. In striking contrast, for the same time the Au content is much higher for the former than that for the latter nanocarrier. It indirectly indicates that AuNR@MSN-HB@LF was preferably internalized by the tumor cells. The reason could be explained that the lipid bilayer in the nanocomposite possesses similar chemical and structural properties with cell membrane, which facilitates cellular uptake of the nanocomposite and enhances following cellular bioavailability by multiple ways such as direct liposome-cell fusion, lipid exchange, phagocytosis, and endocytosis.[55,56] In order to further illustrate that LF has a large influence on the efficient accumulation of the nanocomplex, the process was monitored by flow cytometry. After internalized by MCF-7 cells within the same time, the average fluorescence intensity of the group with LF is higher than that of the group without LF (Fig. 3c). More importantly, as revealed in Fig. 3d, the corresponding relative increase ratio of AuNR@MSN-HB@LF internalized by the tumor cell were considerably higher. Obviously, LF can enhance intracellular accumulation in a shorter time, which supports the following PTT and PDT.

Anticancer Efficiency *in vitro*

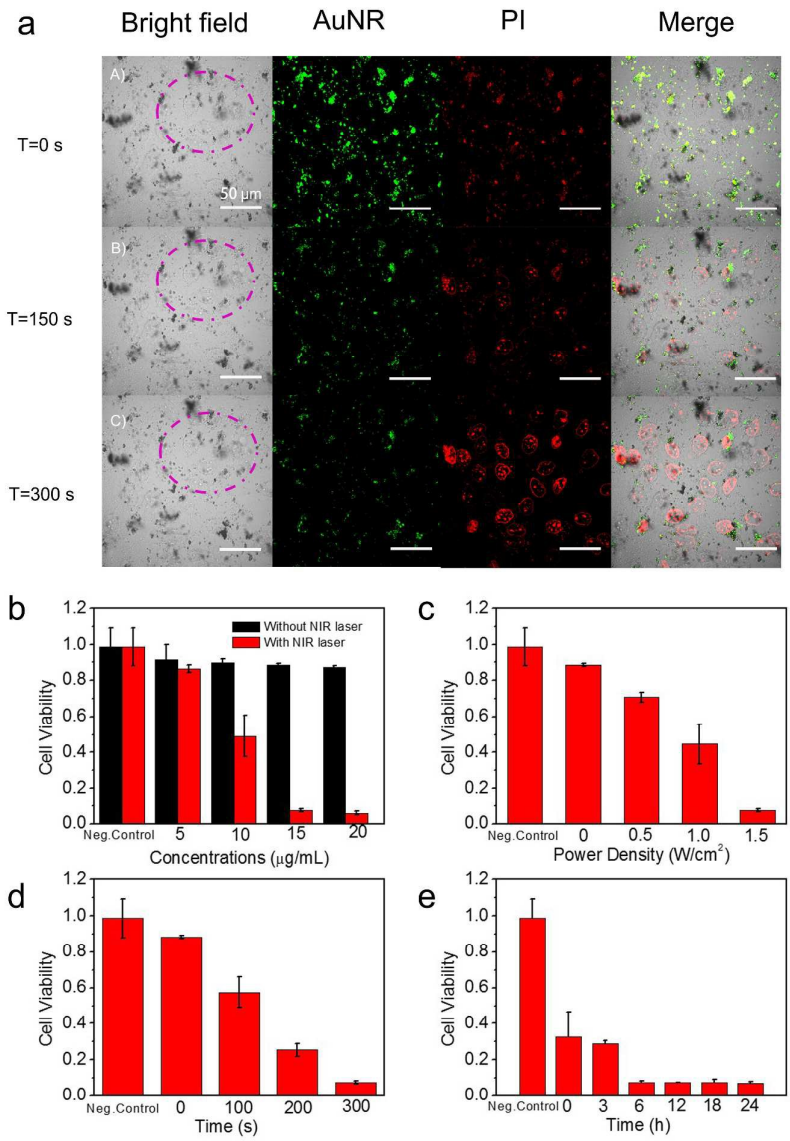

Fig. 4 (a) Two-photon images of MCF-7 cells co-cultured with AuNR@MSN-HB@LF for 6 h under irradiation for different time. (b) Cell viability depended on the bioconjugate concentration and the laser irradiation (n=3) when the power density is 1.5 W/cm^2 and the irradiation time is 300 s. (c) Cell viability depended on laser irradiation power density (n=3) when the bioconjugate concentration is 15 μg/mL and the irradiation time is 300 s. (d) Cell viability depended irradiation time (n=3) when the laser power density is 1.5 W/cm^2 and the bioconjugate concentration is 15 μg/mL. (e) Time-dependent cell viability (n=3) after laser irradiation (808 nm, 1.5 W/cm^2, 300 s). Cells that were incubated in the absence of agents without irradiation were used as control groups. Data indicate means and the standard errors.

To assess the effect of PTT and PDT *in vitro*, the cells with the bioconjugate were irradiated by a two-photon laser at 808 nm. MCF-7 cells were first incubated with AuNR@MSN-HB@LF for 24 h and then irradiated at different power densities. As shown in Fig. 4a, time-dependent microscopy images exhibit that after one-time illumination for 5 min at a power density of 0.16 mW/cm^2, most cells were killed. In detail, the two-photon luminescence from AuNR can be found in the green channel. With increase of the irradiation time, the intensity of the green fluorescence becomes weaker and weaker. It might be attributed to localized concentration reduction of the nanocomplex mediated by heat-induced diffusion. Additionally, bubbles (shown in the purple circle) were observed in the cell membrane, which presumably results

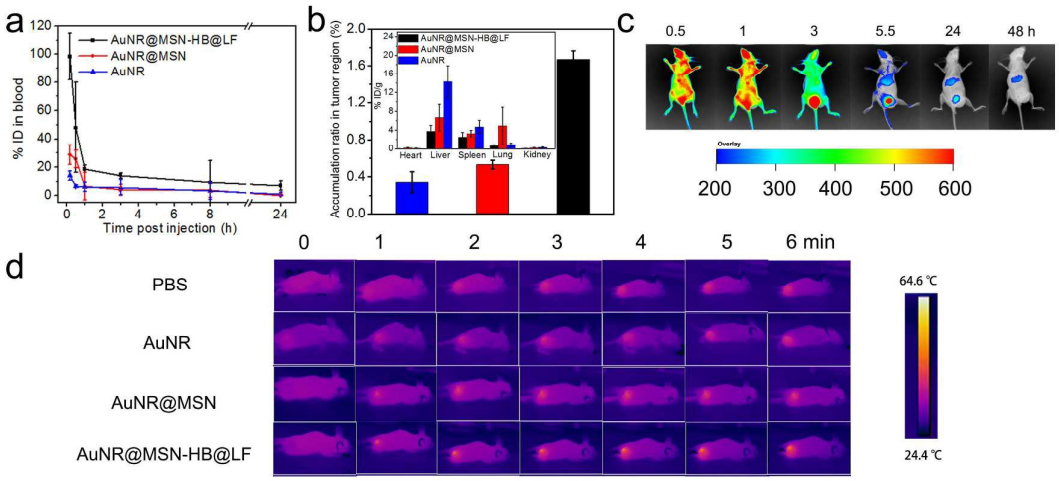

Fig. 5 (a) Blood circulation time of AuNR@MSN-HB@LF, AuNR@MSN, and AuNR analyzed by measuring the Au content in blood by ICP-MS (data expressed as percentage of the injected dose (% ID)). (b) The accumulation ratio of the three nanoparticles above in tumor region. The inset is the biodistribution of nanoparticles at 24 h after administration by measuring the Au content in blood by ICP-MS. (data expressed as percentage of the injected dose per gram of tissue (% ID/g). (c) AuNR@MSN-HB@LF labelled with *cy7* at different time intervals by the living animal imaging. Data indicate means and the standard errors. (d) Infrared thermal images of the tumor bearing mice exposed to an 808 nm laser (1.3 W/cm^2).

from the increased temperature.[57] In contrast, the red signal from propidium iodide (PI) staining the nuclei of dead cells becomes stronger and stronger. The result implies that the tumor cells were killed or damaged under irradiation. In detail, when the bioconjugate was irradiated, AuNR-mediated hyperthermia could be generated to kill the cells. Meanwhile, HB in the bioconjugate could be induced to generate ROS, leading to further cellular damage. As a comparison, cells in the absence of the bioconjugate show no noticeable morphological change after the same laser exposure (Fig. S10†).

The treatment effect *in vitro* was further quantified through a CCK-8 assay by changing the concentration of the bioconjugate, exposure time, and irradiation power density, respectively. MCF-7 cells were seeded in a 96-well plate at 5×10^4 cells/mL per well. The bioconjugate with different concentrations were co-cultured with tumor cells for 24 h. Each well was exposed to laser irradiation (808 nm, 1.5 W/cm^2, 300 s). Then, the cells were washed with fresh culture medium and further incubated for 24 h for apoptosis and necrosis to take place. As shown in Fig. 4b, the cell death was enhanced with the increased concentration. In particular, 92.5±0.8% of the cells were killed when the concentration of nanocomplex is 15 μg/mL. As a comparison, the bioconjugate shows no obvious toxicity to the cells under darkness. Moreover, as expected, the cell viability decreases with the increasing irradiation time and the power density (Fig. 4c, d). Importantly, as shown in Fig. 4e, there is no apparent change of cell viability during 24 h after laser illumination. The results clearly demonstrate that the nanocomplex combining PDT and PTT provides cancer therapy with higher efficiency *in vitro*, which could be attributed to their sygnerstic effect.

Biodistribution and Antitumor Efficiency *in vivo*

Before evaluation of the anticancer efficiency of the nanocomplex *in vivo*, the blood circulation time of the nanocomplex was studied. In order to investigate the retention time of AuNR, AuNR@MSN and AuNR@MSN-HB@LF in the blood circulation *in vivo*, 100 μL of blood at different time points post administration were collected. After analysis of the Au content in the blood by ICP-MS, as shown in Fig. 5a, the blood circulation time of AuNR@MSN-HB@LF is longer than that of AuNR and AuNR@MSN. The content of AuNR and AuNR@MSN decreases so quickly that they are almost completely cleared up from the blood at 30 min post administration. In contrast, AuNR@MSN-HB@LF remains. The half-life time in blood circulation is up to about 1 h. The reason may be that after shielding with LF, the particles opsonized by blood proteins and phagocytized by macrophages were reduced.[58] It is important for the nanocomplex to stay much longer time in the blood, which facilitates the efficient accumulation in the tumor region by enhanced permeability and retention (EPR) effect-mediated passive or folic acid-induced active delivery.[37, 59-64] Furthermore, to examine the distribution of these nanoparticles in main organs, all groups were sacrificed at 24 h post administration. The tissues (heart, liver, spleen, lung, kidney and tumor) were collected and studied by ICP-MS analysis. As shown in Fig. 5b, after 24 h, compared to two other experimental groups, AuNR@MSN-HB@LF possesses much higher accumulation ratio in the

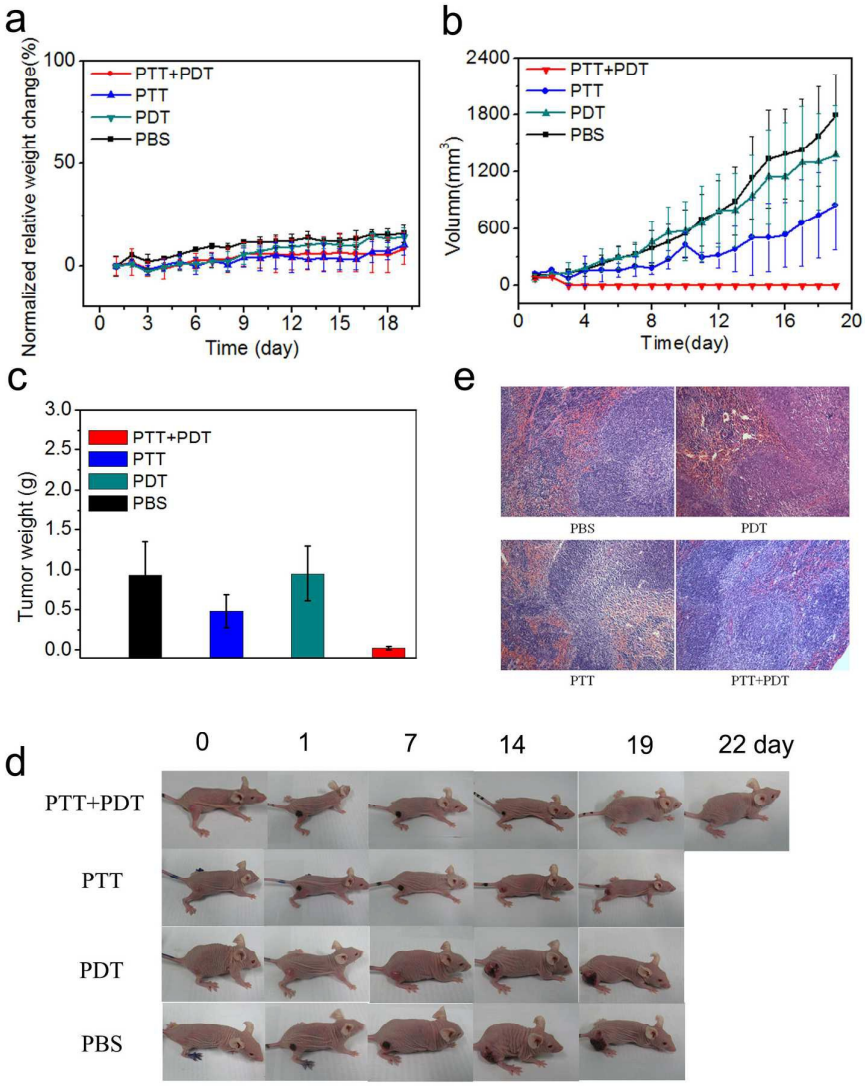

Fig. 6 *In vivo* antitumor activity in the nude mice model with the murine 4T1 breast tumor after injection accompanied by different therapies. (a) Normalized relative body weight change and (b) tumor volume after treatment. (c) The 19-day weight of the 4T1 breast tumor after treatment. Data indicate means and standard errors. (d) Representative photographs of the tumor bearing mice at different time after treatment. (e) Representative 19-day images of the hematoxylin-eosin (HE) section of the typical organ tissue (spleen) after treatment.

tumor region, which can be ascribed to the introduction of LF in the nanocarrier. Meanwhile, the inset in Fig. 5b shows that large amount of AuNR and AuNR@MSN retained in liver, spleen and lung, while the content of AuNR@MSN-HB@LF was much lower in all organs above. Less deposition of the nanocomplex in the organs is very useful for the application in PTT/PDT *in vivo* to minimize side effects. Based on the results above, the nanostructure assembled has the striking advantages of a relatively longer blood circulation time and higher accumulation in the tumor region.

To visually illustrate the effective accumulation *in vivo*, the nanocomplex was labelled by *cy7* (a dye in NIR region) to overcome the limitation of the penetration depth.[65] When the volume of tumors was above 100 mm^3, AuNR@MSN-HB@LF labelled with *cy7* was intravenously injected through the tail vein into the mice bearing the tumor. Monitored at 5.5 h post administration, the fluorescence signals significantly increase and are mainly concentrated in the tumor region (Fig. 5c). This proves the effective accumulation of the nanocomplex. Moreover, the signals of *in vivo* imaging remained for almost 6 h. In addition, the PTT efficiency *in vivo* was recorded by using an infrared thermal camera. As shown in Fig. 5d, the temperature for the AuNR@MSN-HB@LF group is increased by about 10 ^{o}C while the temperature for the other three groups

of AuNR, AuNR@MSN, and PBS is increased by only 5, 6.3 and 3.9 °C, respectively. This is due to higher accumulation of the nanocomplex in the tumor region.

To evaluate the efficiency of the combination therapy of PTT and PDT *in vivo*, when the volume of tumors exceeded 100 mm^3, PBS, AuNR, LF-HB and AuNR@MSN-HB@LF were intravenously injected into female BALB/c nude mice, respectively. After 6 h post administration, the tumors of the mice were irradiated. After 19 days, through normalization shown in Fig. 6a, after combined phototherapy, less body weight change (+8.6%) displays compared to those in the other groups (PBS group: +15.8%; PDT group: +14.2%; PTT group: +10.3%). In addition, as revealed in Fig. 6b, the corresponding tumor volume after combined phototherapy is close to 0 mm^3. In contrast, those in the other groups increase to about 1770 mm^3 (PBS group), 1560 mm^3 (PDT group) and 840 mm^3 (PTT group), respectively. Moreover, Fig. 6c shows the tumor weight in the four groups, indicating the tumor after combined phototherapy nearly disappeared. Furthermore, within 22 days monitoring (Fig. 6d), the combined therapy group exhibits much higher efficiency than the other groups, since tumor tissues almost disappeared after 19 days. Meanwhile, the tumor was almost completely inhibited without any recurrence. The results suggest that the combination therapy of PTT and PDT has a great synergistic effect on inhibiting the tumor growth *in vivo*, which offers a bright prospect for anti-cancer treatment. The histopathological examinations of the tissues (heart, liver, spleen, lung, kidney and tumor) after phototherapy were also performed, as shown in Fig. S11†. All groups showed no obvious pathological changes in heart, liver, lung and kidney, respectively. For the control group and individual therapy groups, the white pulp of the spleen was increased and cell apoptosis appeared (Fig. 6e). Meanwhile, the medullary sinus in the red pulp was expanded and extramedullary hematopoiesis was obvious. The image shows that the necrosis malignant tumor cells were in the afflicted region. In sharp contrast, in combined therapy group, there are no obvious spleen metastases. Note that the slight edema of the liver cell indicated by the dense blue staining might be induced by the nanocomplex accumulation.[47, 66] These results indicate there are obvious advantages of the nanocomplex for combined tumor phototherapy.

Experimental

Materials

Hydrogen tetrachloroaurate (III) trihydrate ($HAuCl_4 \bullet 3H_2O$), sodium borohydride ($NaBH_4$), silver nitrate ($AgNO_3$), L-ascorbic acid (AA), sodium hydroxide (NaOH), hydrochloric acid (HCl), anhydrous chloroform, methanol, and ethanol were purchased from Beijing Chemical Reagent Co., China. Cetyltrimethylammonium bromide (CTAB), tetraethyl orthosilicate (TEOS), deuteroxide (D_2O), (3-aminopropyl) triethoxysilane (APTES), fluorescein isothiocyanate isomer I (FITC-I), propidium iodide (PI) and cholesterol were purchased from Sigma Aldrich. *Cy7* dye was obtained from Beijing Biodee Biotechnology Corporation Ltd., China. 9,10-diphenylanthracene (DPA) was from Alfa Aesar China (Tianjin) Co., Ltd. 1, 2-dioleoyl-sn-glycero-3-phosphoethanolamine (DOPE), 1, 2-dioleoyl-3-trimethylammonium-propane (chloride salt) (DOTAP) and 1, 2-distearoyl-sn-glycero-3-phosphoethanolamine-N-[folate (polyethylene glycol)-2000] (ammonium salt) (DSPE-PEG (2000)-Folate) were purchased from Avanti Polar Lipids (Alabaster, AL, USA). Hypocrellin B (HB) was provided by Prof. Jingquan Zhao at Institute of Chemistry, Chinese Academy of Sciences. Cell counting kit-8 (CCK-8) was purchased from DOJINDO Co., Ltd., Japan. Penicillin, streptomycin, dulbecco's modified eagle medium (DMEM), and fetal bovine serum (FBS) were obtained from Invitrogen. All other materials were commercially available and used as received unless otherwise mentioned. The water with a resistivity of 18.2 MΩ•cm, used throughout the experiment, was purified with a Milli-Q system from Millipore Co., USA.

Preparation of AuNRs

AuNRs were prepared by a seed-mediated growth method.[41, 42] First, Seed solution. 1.5 mL of 0.1 M CTAB solution was mixed with 50 μL of 0.01 M $HAuCl_4$. An ice-cold $NaBH_4$ solution (120 μL, 0.01 M) was added fast under the vigorous stirring that resulted in the formation of a brownish-yellow solution. The seed solution was incubated at 28 °C. Second, Growth solution. 80 mL of 0.1 M CTAB solution was mixed with 4 mL of 0.01M $HAuCl_4$ and 1 mL of 0.01 M $AgNO_3$. Then, 0.8 mL of 0.1 M ascorbic acid was added slowly under gentle stirring until the solution turned to colorless. After 1 mL of 1 M HCl was added, the seed solution (200 μL) was dropped into the mixed solution. The temperature of the growth solution was kept at 28 °C. The as-prepared AuNRs were washed three times and centrifuged at 9500 rpm for 10 min to remove excess CTAB and other impurities in the supernatant. AuNRs were redispersed in water for further use.

Preparation of AuNR@MSN

AuNRs were coated with a silica layer to form core-shell AuNR@MSN by the Stöber method, which depends on the hydrolysis of TEOS under the alkaline conditions in the presence of AuNRs, which act as seeds, and CTAB acts as the soft template. First of all, 400 μL of 0.1 M NaOH was added to AuNRs solution and stirred mildly for 2 hours. Next, 120 μL of 20% TEOS in MeOH was added to the solution at 30 min intervals for three times. Then, the reaction proceeded at 28 °C for 3 days. The product was washed with MeOH, followed by centrifugation at 9000 rpm for 30 min. After dried under vacuum, AuNR@MSN was added into the acidic MeOH (HCl: 80 μL, 12 M; MeOH: 8 mL) at room temperature. After sonication for 20 min, the mixture was heated in water bath at 65 °C. AuNR@MSN was obtained by washing with MeOH for three times and dried under vacuum.

Preparation of AuNR@MSN-HB

2 mL of 20 μg/mL HB MeOH solution was added to 3 mL of well-dispersed AuNR@MSN MeOH. The mixture was kept in darkness and gently stirred for 4 h at room temperature. The mixture was then washed and centrifuged at 9000 rpm for 30 min to remove excess HB and other impurities in the

supernatant. AuNR@MSN-HB was redispersed in water for further use.

Preparation of Mixed Liposomes

Mixed liposomes composed of DOPE, DOTAP, cholesterol, and mPEG2000-DSPE-Floate with a mass ratio of about 1:1:1:0.05 were prepared by a lipid film hydration and membrane extrusion method. In detail, DOPE (1.0 mg), DOTAP (1.0 mg), cholesterol (1.0 mg), and mPEG2000-DSPE (0.05 mg) were mixed in 1 mL of anhydrous chloroform and 1 mL of MeOH in round-bottom flask. The mixture was dried by rotary evaporation and further dried under vacuum overnight. After hydrating in 3.0 mL of H_2O for 30 min, the lipid mixture was then extruded to form liposomes at the same temperature by following the mini-extruder of the liposome from Avanti Polar Lipids, Inc. The liposomes were kept at 4 ^{o}C in the refrigerator, and the shelf period should be not exceeding one week. The preparation of LF-HB was similar to the above procedure except adding HB MeOH solution (1mg/mL, 1mL) to the mixed lipids chloroform/MeOH solution.

Fabrication of AuNR@MSN-HB@LF

To fabricate AuNR@MSN-HB@LF, the as-prepared liposomes (1 mg/mL, 1 mL) were added to 1 mL of AuNR@MSN-HB dispersion and gently stirred for 3 h, respectively. The obtained dispersion was centrifuged at 9000 rpm for 10 min and washed three times with H_2O. AuNR@MSN-HB@LF was resuspended in H_2O and used as soon as possible.

Characterization

The morphologies of the samples were examined by a JEOL 2100F and a JEOL 1011 TEM working at 200 kV and 100 kV. The elemental components were analyzed by an EDX analyzer (Phoenix) as the TEM accessory. A Hitachi U-3010 spectrophotometer was used to record the UV-vis spectra of various samples. In addition, zeta potential and size distribution were documented by a dynamic light scattering technique (Zetasizer Nano, Malvern). The BET analysis was determined by a Brunauer-Emmett-Teller analyzer (BET, ASAP 2020, Micromeritics Instrument Corporation). Au content was determined by inductively coupled plasma mass spectrometry (PerkinElmer, Waltham, MA, U.S.A.). The quantitative analysis of endocytosis was conducted by flow cytometry (FACS Culibur, BD). The thermographs were measured by a FLIR E40 compact infrared (IR) thermal imaging camera (FLIR Systems, U.S.A.). One-photon and two-photon fluorescence images were obtained by a confocal microscope (Olympus FV1000) equipped with a femtosecond NIR laser (808 nm, Spectra-Phsics Mai Tai DeepSee). The curves of the temperature under the NIR laser irradiation were detected by a fast and accurate thermometer (SENDAE, DAE-905T). The ESR spectra were measured by using a Bruker model ESP 300 spectrometer operating at room temperature. The pathological sections were observed by a camera (CoolSNAP). The imaging by *in vivo* fluorescence microscopy was conducted using a Maestro 2 multispectral small-animal imaging system (Kodak In-Vivo imaging system FX Pro).

BET Analysis of AuNR@MSN

More than 100 mg AuNR@MSN was prepared for the analysis. The surface area and the pore size distribution were calculated by the Brunauer-Emmett-Teller (BET) method.

Photothermal Measurements

For concentration-dependent photothermal measurements, a thermometer that allows thermal detection with an accuracy of 0.01 ^{o}C was used. AuNR@MSN-HB@LF with different concentrations (0, 12.5, 25, 50, 75 and 100 μg/mL) was placed in plastic cubes (2 mL) and then irradiated by the NIR laser (808 nm, 1.5 W/cm^2, 300 s). The changes of temperature were immediately measured, and each group was measured for three times. For laser power density-dependent photothermal measurements were performed by the same method. Power density was set at 0.25, 0.5, 0.75, 1.0, 1.25, and 1.5 W/cm^2, respectively.

Thermal Camera Measurement of Temperature

For concentration-dependent photothermal measurements, an infrared thermal camera was used to take pictures of the temperature change. AuNR@MSN-HB@LF with different concentrations (0, 12.5, 25, 50, 75 and 100 μg/mL) was placed in plastic cubes (2 mL) and then irradiated by the NIR laser (808 nm, 1.5 W/cm^2, 300 s). The changes of temperature were recorded every 30 s.

ESR Measurements

The spin trap agent, DMPO reacts with ROS forming the stable DMPO-hydroxyl radical spin adduct DMPO-OH, which produces a typical ESR signal. Photo-induced ESR spectra were obtained by mixing 20 μL of DMPO/acetonitrile with 100 μL of AuNR@MSN-HB@LF which was dispersed in D_2O. AuNR@MSN-HB@LF was then injected into quartz capillaries designed for ESR analysis and O_2 was blown for 3 min to make sure it is saturated with O_2. After that, it was irradiated. Parameter settings: microwave power, 10.09 mW; frequency, 9.8 GHz; time constant, 40.96 ms; scan width, 100 G. The ESR signal generated by AuNR@MSN-HB@LF in the presence of DMPO without irradiation was collected as control.

Temperature-Dependent ROS Generation by LF-HB

In a typical measurement, 630 μL of LF-HB in H_2O (1mg/mL) was mixed with 25 μL of DPA stock solution in DMSO (1mg/mL) in a sealed quartz cuvette. The mixture was put in a water bath at 30, 40, 50, and 60 ^{o}C, respectively. The final concentration of HB is 45 μg/mL, and that of DPA is 58 μg/mL. After irradiation for 5 min by a Xe lamp with a narrow spectral region around 475 nm, the suspension was then taken out for UV-vis spectral measurement.

Cell Culture

MCF-7 cells were cultured in DMEM supplemented with 10% FBS, 1% penicillin and streptomycin in a humidified atmosphere of 5% CO_2 at 37 ^{o}C.

Endocytosis Analysis of AuNR@MSN-HB@LF and AuNR@MSN-HB by ICP-MS

MCF-7 cells were cultured in 35 mm glass-bottom Petri dishes at a density of 5×10^4 cells/mL. After 24 h culture in a humidified atmosphere of 5% CO_2 at 37 ^{o}C, the medium was

removed. AuNR@MSN-HB@LF and AuNR@MSN-HB (15 μg/mL) were separately added to the different dishes for the cellular uptake experiment. Cells were incubated for different times (0.5, 1, 3, 6, and 9 h). Cells in each dish were washed gently with PBS for three times, digested with 0.25% trypsin containing 0.02% EDTA. Then the cells were centrifuged for 5 min at 800 rpm and collected. To dilute the nanostructure, 2 mL of aqua regia was added. In the next day, the solution was transferred into the sample glasses. The glasses were heated so that the acids could be evaporated to dryness. The solution was diluted with a solution containing 2% HNO_3 and 1% HCl. A series of gold standard solutions (0, 0.5, 1, 5, 10, 50 ppb) were prepared. Both standard and test solutions were measured by ICP-MS.

Cellular Internalization Analysis by Flow Cytometry

50 μL of APTES was added to AuNR@MSN-HB dispersed in MeOH, and stirred over 4 h. Then, the product was washed with MeOH and centrifuged at 9000 rpm for 30 min. After dried under vacuum, the aminated AuNR@MSN-HB was dispersed in water and the fluorescent dye FITC was added. The solution was adjusted to pH 8-9 using NaOH solution. The mixture was gently stirred for 24 h at room temperature. Then, the product was washed three times with water and centrifuged at 9000 rpm for 10 min. After dried under vacuum, the aminated AuNR@MSN-HB after labelled with FITC was dispersed in water. MCF-7 cells were cultured in a 6-well plate at a density of 5×10^4 cells/mL. The medium was removed after 24 h culture in humidified atmosphere of 5% CO_2 at 37 ^{o}C. AuNR@MSN-HB@LF and AuNR@MSN-HB (15 μg/mL) were separately added to the different wells and co-incubated for different times (0.5, 1, 3, 6, 9 h). Cells in each well were washed gently with PBS for three times, digested with 0.25% trypsin containing 0.02% EDTA. Then the cells were centrifuged for 5 min at 800 rpm and collected. After that, the cells were dispersed in 1 mL of PBS for flow cytometry analysis (FACS Culibur, BD).

Endocytosis Study of AuNR@MSN-HB@LF

With regard to the endocytosis study, 5×10^4 cells/mL MCF-7 cells were grown in 35 mm glass-bottom Petri dishes, supplemented with culture medium at a concentration to allow 90% confluence in 24 h. Then, AuNR@MSN-HB@LF was incubated at 37 ^{o}C in 5% CO_2, 70% humidity environment for 6 h. After that, the cells were washed three times with PBS, and then 1 mL of culture medium and 10 μL of LysoTracker Red were supplemented into the glass-bottom Petri dishes. Finally, the cells were immediately observed with a CLSM using a 60×objective lens (NA 1.35 Oil) and processed using Olympus Fluoview software. Fluorescence and luminescence images were taken by multitrack mode: LysoTracker Red excited by the 559 nm laser was detected mainly in the red channel through an emission filter at 565-615 nm, while two-photon photoluminescence of AuNRs was collected mainly in the green channel through an emission filter at 500-550 nm when excited by the 808 nm two-photon laser.

Two-photon Fluorescence Imaging

MCF-7 cells were grown in 35 mm glass-bottom Petri dishes, supplemented with culture medium at a concentration to allow 90% confluence in 24 h. In the following day, 15 μg/mL of AuNR@MSN-HB@LF was added to each dish. Cells were incubated for 6 h. MCF-7 cells in each well were washed gently with PBS for three times, and then 1.5 mL of PBS and 10 μL of PI were supplemented into the glass-bottom Petri dishes. Finally, the two-photon imaging was taken with a CLSM using a 60×objective lens (NA 1.35 Oil) and processed using Olympus Fluoview software. Two-photon fluorescence was collected using a two-photon laser (Maitai, America) as excitation source.

PTT and PDT *In vitro*

MCF-7 cells were suspended in DMEM and 10% FBS supplemented with 1% penicillin and streptomycin and were seeded in a 96-well culture plate at the density of 5×104/mL and cultured at 37 ^{o}C in 5% CO_2, 70% humidity environment for 24 h. Then AuNR@MSN-HB@LF was added and cells were incubated for another 24 h. After that, cells were washed three times with PBS. The cells were irradiated by an fs-pulse laser (808 nm, 1.5 W/cm^2, 300 s), respectively. Cells without laser irradiation were regarded as control. Cell viability was measured by using CCK-8 (Dojindo Laboratories, Kumamoto, Japan). CCK-8 solution (10 μL) was added to each well, followed by incubation for another 2 h. The absorbance value at 450 nm was measured with a microplate reader (Tecan Infinite M200).

Animal Protocol

All animal experiments were conducted in compliance with the relevant laws and institutional guidelines and approved by the local ethics committee. Balb/c nude mice (Male, 4-6 weeks) were provided by Department of Experimental Animals, Institute of Process Engineering, Chinese Academy of Sciences (Beijing, China). All mice were kept under specific pathogen-free conditions with standard and free water and food. MCF-7 tumor-bearing mice were prepared by hypodermic injection of (subcutaneous injection) a suspension of 1×10^7 MCF-7 cells in PBS (100 μL) into the right legs of female BALB/c nude mice (4-5 weeks old, 16-20 g). Tumor growth was monitored every other day by measurement with a digital vernier caliper and the tumor volume was calculated with the formula: tumor volume = 1/2 (length × width^2). At the same time, the mice were taken photos with a digital camera (Canon PowerShot SX110 IS) and the weight was recorded by the balance.

Blood Circulation Retention Time

To show the blood circulation time of AuNR, AuNR@MSN and AuNR@MSN-HB@LF, 200 μL of suspensions with the same Au content were intravenously injected into female BALB/c nude mice from the tail vein. The blood samples were collected from the eyes of the mice at 10 min, 30 min, 1 h, 3 h, 8 h and 24 h post administration, and stored at -20 ^{o}C before ICP-MS analysis. Otherwise, the mice were sacrificed at 24 h after injection and their organs (heart, liver, spleen, lung, and kidney) and tumors were collected for Au content determination with ICP-MS.

ICP-MS for Au Element Quantification

The above samples were pre-digested overnight with 5.0 mL of aqua regia, and then mixed with 5.0 mL of 30% H_2O_2 and digested for 1 h in beakers on the heating jacket at 350 ^{o}C until the residual v olume decreased to 0.5 mL. Then mixed acid solution of 2% HNO_3 and 1% HCl was added. The Elan DRC II ICP-MS (PerkinElmer, Waltham, MA, U.S.A.) was used to measure the amount of Au in the samples. All test solutions were measured three times by ICP-MS. The amount of Au was finally expressed as the percentage of the injected dose or normalized to the tissue weight per gram.

Imaging *In vivo*

50 μL of APTES was added to AuNR@MSN-HB dispersed in MeOH, stirring over 4 h. Then, the product was washed with MeOH by centrifugation at 9000 rpm for 30 min. After dried under vacuum, the aminated AuNR@MSN-HB was dispersed in water and the fluorescent dye *cy7* (1 mg/mL) was added, according to the previous report.[65] The solution was adjusted to pH 8-9 using NaOH solution. The mixture was gently stirred for 24 h at room temperature. Then, the product was washed with water and centrifuged at 9000 rpm for 10 min. After dried under vacuum, the aminated AuNR@MSN-HB after labelled with *cy7* was dispersed in water. When the tumors reached a volume of about 100 mm^3, 200 μL of AuNR@MSN-HB@LF (2 mg/mL) labelled by *cy7* was intravenously injected into female BALB/c nude mice from the tail. To perform *in vivo* imaging, the mice were first anesthetized with isoflurane by an Animal Aneathesia Ventilator System. Real-time NIR fluorescent images of *cy7* in mice were recorded at various time points after the injection with a Maestro 2 multispectral small-animal imaging system (Kodak In-Vivo imaging system FX Pro) at an excitation wavelength of 710 nm and an emission wavelength of 790 nm.

PTT and PDT *In vivo*

When the tumors reached a volume of about 100 mm3, the tumor-bearing mice were divided into four groups (n=3 per group). Then, 200 μL of PBS, LF-HB (HB content at 45 μg/mL), AuNR (Au content at 840 μg/mL), and AuNR@MSN-HB@LF (2 mg/mL, Au content at 840 μg/mL and HB content at 45 μg/mL) were intravenously injected into female BALB/c nude mice from the tail, respectively. At 6 h post administration, all groups were exposed to laser irradiation under the same condition. The changes of the temperature in the tumor region were recorded by the IR camera. After irradiation, the tumor growth was monitored the following 19 days. To evaluate the therapeutic efficacy of different groups, the mice were sacrificed and the tumors were dissected and weighed. The different tissues (heart, liver, spleen, kidney, lung, and tumor) were collected for the biochemical analysis and histopathological examination.

Histopathology

On the 19th day after injection and irradiation, one mouse was selected randomly and sacrificed for histological analysis. The tumors and organs including heart, liver, spleen, lung, and kidney were fixed with 10% neutral buffered formalin. The histopathological tests were performed according to standard laboratory procedures. Tissue samples were numbered and given blind to the pathologist for conventional processing and analysis. Briefly, the tissue samples were dehydrated by treating with gradient concentration of alcohol, then, embedded in paraffin blocks, sectioned into 5 μm slices, and mounted onto the glass slides. After hematoxylin-eosin (HE) staining, the sections were observed, and images were taken using an optical microscope. (Magnification: liver, heart, spleen, lung, and kidney×100)

Statistical Analysis

At least three parallel experiments were conducted for each sample. The data were processed by Origin 8.0.

Conclusions

In summary, we rationally construct a biointerfaced nanocomplex with core@shell nanostructures by coating AuNR@MSN-HB with LF, which can combine PTT with PDT in a one-time synergistic manner under NIR two-photon illumination. The modification by LF allows the nanocomplex to be internalized by the tumor cells much more effectively. After illumination, AuNR in this bioconjugate can convert light energy to heat and HB can induce O_2 to produce ROS for PDT. Remarkably, increased temperature can enhance the production of ROS. In addition, the bioconjugate shows minimal cytotoxicity and high biocompatibility in darkness. Furthermore, AuNR@MSN-HB@LF mediated synergistic PTT and PDT can significantly enhance the treatment efficiency *in vivo*, leading to superior tumor eradiation. Moreover, the phototherapy above does not exhibit obvious toxicity on major organs. Therefore, the NIR photoinduced active and selective anticancer treatment represents a facile external control and outstanding practical efficacy. It is expected that the well-defined nanostructures can be further armoured with other drugs or NIR responsive materials for the optimal therapy.

Acknowledgements

We acknowledge the financial support of this research by the National Nature Science Foundation of China (21320102004, 21273250, 21433010 and 21321063), and National Basic Research Program of China (973 program, No. 2013YQ160551).

Notes and references

1 Z. J. Zhang, J. Wang, X. Nie, T. Wen, Y. L. Ji, X. C. Wu, Y. L. Zhao, C. Y. Chen, *J. Am. Chem. Soc*. 2014, **136**, 7317-7326.
2 P. Huang, L. Bao, C. L. Zhang, J. Lin, T. Luo, D. P. Yang, M. He, Z. M. Li, G. Gao, B. Gao, S. Fu, D. X. Cui, *Biomaterials* 2011, **32**, 9796-9809.
3 C. L. Du, J. Zhao, J. B. Fei, L. Gao, W. Cui, Y. Yang, J. B. Li, *Chem. Asian J*. 2013, **8**, 736-742.
4 N. N. Wang, Z. L. Zhao, Y. F. Lv, H. H. Fan, H. R. Bai, H. M. Meng, Y. Q. Long, T. Fu, X. B. Zhang, W. H. Tan, *Nano Res*. 2014, **7**, 1291-1301.

5 L. Gao, J. B. Fei, J. Zhao, H. Li, Y. Cui, J. B. Li, *ACS Nano* 2012, **6**, 8030-8040.
6 D. G. Wang, Z. A. Xu, H. J. Yu, X. Z. Chen, B. Feng, Z. R. Cui, B. Lin, Q. Yin, Z. W. Zhang, C. Y. Chen, J. Wang, W. Zhang, Y. P. Li, *Biomaterials* 2014, **35**, 8374-8384.
7 M. Q. Chua, H. K. Li, Q. Wu, F. J. Wo, D. L. Shi, *Biomaterials* 2014, **35**, 8357-8373.
8 P. Vijayaraghavan, C. H. Liu, R. Vankayala, C. S. Chiang, K. C. Hwang, *Adv. Mater*. 2014, **26**, 6689-6695.
9 F. Greco, M. J. Vicent, *Adv. Drug Deliver. Rev*. 2009, **61**, 1203-1213.
10 Z. H. Sheng, D. H. Hu, M. B. Zheng, P. F. Zhao, H. L. Liu, D. Y. Gao, P. Gong, G. H. Gao, P. F. Zhang, Y. F. Ma, L. T. Cai, *ACS Nano* 2014, **8**, 12310-12322.
11 W. W. Zhang, Y. Q. Wang, X. Y. Sun, W. H. Wang, L. X. Chen, *Nanoscale* 2014, **6**, 14514-14522.
12 M. Lin, Y. Q. Wang, X. Y. Sun, W. H. Wang, L. X. Chen, *ACS Appl. Mater. Interfaces* 2015, **7**, 7516-7525.
13 E. L. Samuel, C. J. Murphy, *J. Am. Chem. Soc*. 2012, **134**, 15607-15620.
14 A. M. Alkilany, L. B. Thompson, S. P. Boulos, P. N. Sisco, C. J. Murphy, *Adv. Drug Deliver. Rev*. 2012, **64**, 190-199.
15 X. H. Huang, I. H. El-Sayed, W. Qian, M. A. El-Sayed, *J. Am. Chem. Soc*. 2006, **128**, 2115-2120.
16 X. H. Huang, P. K. Jain, I. H. El-Sayed, M. A. El-Sayed, *Laser Med. Sci*. 2008, **23**, 217-228.
17 M. F. Tsai, S. H. Chang, F. Y. Cheng, V. Shanmugam, Y. S. Cheng, C. H. Su, C. S. Yeh, *ACS Nano* 2013, **7**, 5330-5342.
18 E. B. Dickerson, E. C. Dreaden, X. H. Huang, I. H. El-Sayed, H. H. Chu, S. Pushpanketh, J. F. McDonald, M. A. El-Sayed, *Cancer Lett*. 2008, **269**, 57-66.
19 J. H. Park, G. von Maltzahn, M. J. Xu, V. Fogal, V. R. Kotamraju, E. Ruoslahti, S. N. Bhatia, M. J. Sailor, *Proc. Natl. Acad. Sci. U. S. A.* 2010, **107**, 981-986.
20 J. Chen, D. Wang, J. Xi, L. Au, A. Siekkinen, A. Warsen, Z. Y. Li, H. Zhang, Y. Xia, X. Li, *Nano Lett.* 2007, **7**, 1318-1322.
21 J. Chen, C. Glaus, R. Laforest, Q. Zhang, M. Yang, M. Gidding, M. J. Welch, Y. Xia, *Small* 2010, **6**, 811-817.
22 N. W. S. Kam, M. O'Connell, J. A. Wisdom, H. J. Dai, *Proc. Natl. Acad. Sci. U. S. A.* 2005, **102**, 11600-11605.
23 H. K. Moon, S. H. Lee, H. C. Choi, *ACS Nano* 2009, **3,** 3707-3713.
24 J. T. Robinson, K. Welsher, S. M. Tabakman, S. P. Sherlock, H. L. Wang, R. Luong, H. J. Dai, *Nano Res*. 2010, **3,** 779-793.
25 K. Yang, S. Zhang, G. Zhang, X. Sun, S. T. Lee, Z. Liu, *Nano Lett*. 2010, **10**, 3318-3323.
26 J. T. Robinson, S. M. Tabakman, Y. Y. Liang, H. L. Wang, *J. Am. Chem. Soc*. 2011, **133**, 6825-6831.
27 M. Li, X. Yang, J. Ren, K. Qu, X. Qu, *Adv. Mater*. 2012, **24**, 1722-1728.
28 Z. M. Markovic, L. M. Harhaji-Trajkovic, B. M. Todorovic-Markovic, D. P. Kepic, K. M. Arsikin, S. P. Jovanovic, A. C. Pantovic, M. D. Dramicanin, V. S. Trajkovic, *Biomaterials* 2011, **32**, 1121-1129.
29 J. Lin, S. J. Wang, P. Huang, Z. Wang, S. H. Chen, G. Nie, W. W. Li, J. He, D. X. Cui, G. M. Lu, X. Y. Chen, Z. H. Nie, *ACS Nano* 2013, **7**, 5320-5329.
30 R. Vankayala, C. C. Lin, P. Kalluru, C. S. Chiang, K. C. Hwang, *Biomaterials* 2014, **35**, 5527-5538.
31 B. K. Wang, J. H. Wang, Q. Liu, H. Huang, M. Chen, K. Y. Li, C. Z. Li, X. F. Yu, P. K. Chu, *Biomaterials* 2014, **35**, 1954-1966.
32 X. Huang, X. J. Tian, W. L. Yang, B. Ehrenberg, J. Y. Chen, *Phys. Chem. Chem. Phys*. 2013, **15**, 15727-15733.
33 B. Jang, J. Y. Park, C. H. Tung, I. H. Kim, Y. Choi, *ACS Nano* 2011, **5**, 1086-1094.
34 Z. Z. Shi, W. Z. Ren, A. Gong, X. M. Zhao, Y. H. Zou, E. M. B. Brown, X. Y. Chen, A. G. Wu, *Biomaterials* 2014, **35**, 7058-7067.
35 J. Wang, M. X. You, G. Z. Zhu, M. I. Shukoor, Z. Chen, Z. L. Zhao, M. B. Altman, Q. Yuan, Z. Zhu, Y. Chen, C. Z. Huang, W. H. Tan, *Small* 2013, **9**, 3678-3684.
36 J. Wang, G. Z. Zhu, M. X. You, E. Q. Song, M. I. Shukoor, K. J. Zhang, M. B. Altman, Y. Chen, Z. Zhu, C. Z. Huang, W. H. Tan, *ACS Nano* 2012, **6**, 5070-5077.
37 C. Ayala-Orozco, C. Urban, M. W. Knight, A. S. Urban, O. Neumann, S. W. Bishnoi, S. Mukherjee, A. M. Goodman, H. Charron, T. Mitchell, M. Shea, R. Roy, S. Nanda, R. Schiff, Naomi J. Halas, A. Joshi, *ACS Nano* 2014, **8**, 6372-6381.
38 Y. Y. Xu, J. Wang, X. F. Li, Y. Liu, L. R. Dai, X. C. Wu, C. Y. Chen, *Biomaterials* 2014, **35**, 4667-4677.
39 H. Sun, J. T. He, J. Y. Wang, S. Y. Zhang, C. C. Liu, T. Sritharan, S. Mhaisalkar, M. Y. Han, D. Wang, H. Y. Chen, *J. Am. Chem. Soc*. 2013, **135**, 9099-9110.
40 S. Kim, T. Y. Ohulchanskyy, H. E. Pudavar, R. K. Pandey, P. N. Prasad, *J. Am. Chem. Soc*. 2007, **129**, 2669-2675.
41 B. Nikoobakht, Z. L. Wang, M. A. El-Sayed, *J. Phys. Chem. B*. 2000, **104**, 8635-8640.
42 L. M. Wang, X. Y. Lin, J. Wang, Z. J. Hu, Y. L. Ji, S. Hou, Y. L. Zhao, X. C. Wu, C. Y. Chen, *Adv. Funct. Mater.* 2014, **24**, 4229-4239.
43 Y. Roiter, M. Ornatska, A. R. Rammohan, J. Balakrishnan, D. R. Heine, S. Minko, *Langmuir* 2009, **25**, 6287-6299.
44 E. Sackmann, *Science* 1996, **271**, 43-48.
45 S. Savarala, S. Ahmed, M. A. Ilies, S. L. Wunder, *Langmuir* 2010, **26**, 12081-12088.
46 Z. J. Zhang, L. M. Wang, J. Wang, X. M. Jiang, X. H. Li, Z. J. Hu, Y. L. Ji, X. C. Wu, C. Y. Chen, *Adv. Mater*. 2012, **24**, 1418-1423.
47 M. B. Zheng, C. X. Yue, Y. F. Ma, P. Gong, P. F. Zhao, C. F. Zheng, Z. H. Sheng, P. F. Zhang, Z. H. Wang, L. T. Cai, *ACS Nano* 2013, **7**, 2056-2067.
48 V. P. Chauhan, T. Stylianopoulos, J. D. Martin, Z. PopoviA, O. Chen, W. S. Kamoun, M. G. Bawendi, D. Fukumura, R. K. Jain, *Nat. Nanotechnol*. 2012, **7**, 383-388.
49 S. Dzwigaj, H. Pezerat, *Free Radical Res*.1995, 23, 103-115.
50 C. L. Yu, S. Chen, M. H. Zhang, T. Shen, *Photochem. Photobiol.* 2001, **73**, 482-488.
51 L. Gao, R. Liu, F. P. Gao, Y. L. Wang, X. L. Jiang, X. Y. Gao, *ACS Nano* 2014, **8**, 7260-7271.
52 M. Hoebeke, H. J. Schuitmakerz, L. E. Janninkz, T. Dubbelman, A. Jakobsl, A. VandeVorst, *Photochem. Photobiol*. 1997, **66**, 502-508.
53 R. Di Corato, G. Bealle, J. Kolosnjaj-Tabi, A. Espinosa, O. Clement, A. K. A. Silva, C. Menager, C. Wilhelm, *ACS Nano* 2015, **9**, 2904-2916.
54 M. R. K. Ali, S. R. Panikkanvalappil, M. A. El-Sayed, *J. Am. Chem. Soc.* 2014, **136**, 4464-4467.
55 M. H. Li , C. Teh, C. Y. Ang, S. Y. Tan, Z. Luo, Q.Y. Qu, Y. Y. Zhang, V. Korzh, Y. L. Zhao, *Adv. Funct. Mater.* 2015, **25**, 5602-5610.
56 V. P. Torchilin, *Nat. Rev. Drug Discovery* 2005, **4**, 145.
57 L. Tong, C. M. Cobley, J. Y. Chen, Y. N. Xia, J. X. Cheng, *Angew. Chem. Int. Ed*. 2010, **49**, 3485-3488.
58 V. P. Chauhan, T. Stylianopoulos, J. D. Martin, Z. PopoviA, O. Chen, W. S. Kamoun, M. G. Bawendi, D. Fukumura, R. K. Jain, *Nat. Nanotechnol.* 2012, **7**, 383-388;
59 P. Huang, D. L. Wang, Y. Su, W. Huang, Y. F. Zhou, D. X. Cui, X. Y. Zhu, D. Y. Yan, *J. Am. Chem. Soc*. 2014, **136**, 11748-11756.
60 C. Wong, T. Stylianopoulos, J. Cui, J. Martin, V. P. Chauhan, W. Jiang, Z. Popovíc, R. K. Jain, M. G. Bawendi, D. Fukumura, *Proc. Natl. Acad. Sci. U. S. A*. 2011, **108**, 2426-2431.
61 S. M. Moghimi, A. C. Hunter, J. C. Murray, *Pharmacol. Rev.* 2001, **53**, 283-318.
62 D. Peer, J. M. Karp, S. Hong, O. C. Farokhzad, R. Margalit, R. Langer, *Nat. Nanotechnol*. 2007, **2**, 751-760.

63 M. E. Davis, Z. Chen, D. M. Shin, *Nat. Rev. Drug Discov.* 2008, **7**, 771-782.
64 J. Barreto, W. O'Malley, M. Kubeil, B. Graham, H. Stephan, L. Spiccia, *Adv. Mater*. 2011, **23**, 18-40.
65 F. Lu, S. H. Wu, Y. Hung, C. Y. Mou, *Small* 2009, **5**, 1408-1413.
66 S. S. Su, Y. H. Tian, Y. Y. Li, Y, P. Ding, T. J. Ji, M. Y. Wu, Y. Wu, G. J. Nie, *ACS Nano* 2015, **9**, 1367-1378.